Accepted Manuscript



Improvement of mechanical behaviors of a superlight Mg-Li base alloy by duplex phases and fine precipitates

Yun Zou, Lehao Zhang, Yang Li, Hongtao Wang, Jiabin Liu, Peter K. Liaw, Hongbin Bei, Zhongwu Zhang

PII: S0925-8388(17)34201-9

DOI: 10.1016/j.jallcom.2017.12.025

Reference: JALCOM 44111

To appear in: *Journal of Alloys and Compounds*

Received Date: 12 July 2017

Revised Date: 1 December 2017

Accepted Date: 4 December 2017

Please cite this article as: Y. Zou, L. Zhang, Y. Li, H. Wang, J. Liu, P.K. Liaw, H. Bei, Z. Zhang, Improvement of mechanical behaviors of a superlight Mg-Li base alloy by duplex phases and fine precipitates, *Journal of Alloys and Compounds* (2018), doi: 10.1016/j.jallcom.2017.12.025.

This is a PDF file of an unedited manuscript that has been accepted for publication. As a service to our customers we are providing this early version of the manuscript. The manuscript will undergo copyediting, typesetting, and review of the resulting proof before it is published in its final form. Please note that during the production process errors may be discovered which could affect the content, and all legal disclaimers that apply to the journal pertain.

ACCEPTED MANUSCRIPT

Improvement of mechanical behaviors of a superlight Mg-Li base alloy by duplex phases and fine precipitates

Yun Zou[1, 2], Lehao Zhang[3], Yang Li[2], Hongtao Wang[4], Jiabin Liu[3], Peter.K. Liaw[5], Hongbin Bei[6], Zhongwu Zhang[1,*]

[1]*Key Laboratory of Superlight Materials and Surface Technology, Ministry of Education, College of Materials Science and Chemical Engineering, Harbin Engineering University, Harbin 150001, P R China*

[2]*School of Mechanical Engineering, Zhengzhou University, Zhengzhou 450001, P R China*

[3]*School of Materials Science and Engineering, Zhejiang University, Hangzhou 310027, P R China*

[4]*Institute of Applied Mechanics, Zhejiang University, Hangzhou 310027, P R China*

[5]*Department of Materials Science and Engineering, University of Tennessee, Knoxville, TN 37996, USA*

[6]*Materials Science and Technology Division, Oak Ridge National Laboratory, TN 37831, USA*

Abstract: Limitations of strength and formability are the major obstacles to the industrial application of magnesium alloys. Here, we demonstrate, by producing the duplex phases and fine intermetallic particles in composition-optimized superlight Mg-Li-Al alloys, a unique approach to simultaneously improve the comprehensive mechanical properties (a strength-ductility balance). The phase components and microstructures, including the size, morphology, and distribution of precipitated-intermetallic particles can be optimized by tuning the Li content, which strongly influences the work-hardening behavior and tension-compression yield asymmetry.

Keywords: Mg-Li alloy; Mechanical properties; Work-hardening; Tension-compression yield asymmetry

*Corresponding authors:

Email: zwzhang@hrbeu.edu.cn; Tel: +86-451-82568591 (Zhongwu Zhang)

1. Introduction

Limitations of strength and formability are the major obstacles to the industrial application of magnesium (Mg) alloys. The poor room-temperature formability of Mg comes from the hexagonal-close-packed (hcp) crystal structure due to the scarcity of easy slip systems [1-4]. Because of the low density of lithium (0.58 g/cm^3) and its ability to form the body-center-cubic (bcc) structured Mg (Li) solid solution phases, alloying with Li yields the lightest Mg-Li alloy [5] with the significantly-improved malleability, which is essential for structural applications, such as automotive, aerospace, and electronic industries [6]. According to the Mg-Li binary phase diagram [7], alloying Mg with Li can also change the crystal structure of Mg. The Mg-Li alloy retains the hcp structure (a α phase), when the Li content is less than 5 weight percent (wt. %), which shows a moderate strength and a limited formability. The bcc structure (a β phase) is formed when the Li content is above 11 wt. %, which effectively improves the ductility but notably lowers the strength. Between 5 to 11 wt. % of Li contents, the hcp structure and bcc structure co-exist, leading to an interesting compromise by combining the moderate strength of the α phase with the excellent ductility of the β phase. Moreover, even in the hcp region, the addition of Li can reduce the axial ratio of c/a in Mg and increase stacking-fault energy (SFE), which promotes non-basal slips, and, hence, provides additional deformation modes other than basal slip [8-10].

Although alloying Li in Mg can effectively improves the ductility, the disadvantage of alloying Li in Mg alloys making the material strength too low to meet the practical industrial application [5, 11]. To overcome this disadvantage, alloying with Al, Zn, RE, etc., is one of the most effective methods to improve the mechanical properties [5, 8, 11, 12] by means of solid-solution hardening and the formation of intermetallic-compound reinforcements. Among them, Al has a great potential in effectively increasing the strength without damaging the lightweight due to the high solubility of Al in Mg-Li alloys [5] and low density. Lentz et al. [8] found that the addition of 1 wt. % Al in the extruded Mg-4 wt. % Li increases the yield strength in

both tension and compression by 30%, which is a consequence of an increase in the resistance to slip combining a decrease in the resistance to $\{10\bar{1}2\}\langle 10\bar{1}\bar{1}\rangle$ twinning. A comparative study on Mg-4Li, Mg-4Li-3Al, and Mg-4Li-5Al (in wt. %) by Trojanová et al. [13] has also showed that the addition of Al to the Mg-4Li alloy increases the alloy strength.

The work/strain hardening behavior, which influences both strength and ductility, is one of the important parameters to understand the plastic deformation of materials [14, 15]. Previous studies performed on Mg-Li alloys [14, 15] were mainly focused on the Mg-Li-Zn (LZ) alloys. Wu et al. [14] have studied the plastic anisotropy and work-hardening behavior of the cold-rolled dual-phase Mg-(6, 9)Li-1Zn alloys with two Li contents. The results showed that the stage-II strain-hardening rate in the cold-rolled Mg-6Li-1Zn (LZ61) alloy sheet, which can be related to the evolution of long-range stresses, is caused by the dislocation pile-ups at the interface of the β-particle. However, no stage-II linear hardening behavior is exhibited in the cold-rolled Mg-9Li-1Zn (LZ91) alloy sheet because an earlier onset of dynamic recovery occurs. Wu et al. [16] also reported that the heat treatment performed on the extruded β phase Mg-10.31Li-1.03Al-0.47Zn (in wt. %) (LAZ1010) specimen could enhance the work-hardening behavior and, thus, improve the mechanical properties by the age-hardening effect. Karami and Mahmudi [15] have characterized and compared the tensile and shear work-hardening behaviors of the fine-grained Mg-(6, 12)Li-1Zn (in wt. %) alloys, and the results were similar to that of the Mg-(6, 9)Li-1Zn (in wt. %) [14]: the stages II and III of the classical Kocks-Mecking plot (the strain-hardening rate versus net flow stress) were seen in the extruded condition of the Mg-6Li-1Zn (in wt. %) (LZ61) alloy but no stage-II was observed in the bcc Mg-12Li-1Zn (in wt. %) (LZ121) alloy due to the SFE improvement caused by a higher Li content of the Mg lattice structure. Thus, the work-hardening behaviors of the α phase, (α + β) phase and β phase ternary Mg-Li-Al are very attractive.

Here we systemically investigate the effects of the Li content on microstructures, tensile and work-hardening behaviors as well as tension-compression yield asymmetry

of three Mg-Li-Al alloys with the α phase, (α + β) phases, and β phase, by changing the Li concentration.

2. Materials and experiments

2.1. Material preparation

Three ingots with the nominal chemical compositions of Mg-3Li-6Al (LA36), Mg-9Li-6Al (LA96), and Mg-15Li-6Al (LA156) (in wt. %) alloys were prepared under argon atmosphere by induction-melting high-purity elemental metals (99.9 Mg, 99.9 Li, and 99.9 Al, in wt. %). The induction-melted alloy buttons were, then, drop-cast into plates in a copper mold. The actual measured chemical compositions of the as-cast alloys are Mg-3.8Li-6.1Al (LA36), Mg-9.5Li-6.1Al (LA96), and Mg-15.9Li-6.2Al (LA156) (in wt. %), which were determined by the Inductively-Coupled Plasma-Atomic Emission Spectrometry (ICP-AES, Thermo Elemental, IRIS Intrepid II XSP). For comparing the mechanical properties, we also prepared the corresponding Li-containing binary Mg-(3,9,15)Li alloy with the same preparation process. The actual measured chemical compositions of the as-cast binary alloys are Mg-3.9Li, Mg-9.6Li, and Mg-16.0Li (in wt. %), which were also determined by the ICP-AES.

2.2. Microstructural characterization

The microstructures were analyzed using the optical microscopy (OM) and scanning electron microscopy (SEM, JSM-6480A, Japan Electronics), compositions of individual phases of the alloys were examined with the attached energy-dispersive spectroscopy (EDS, INC250, Japan Electronics) and phases were analyzed by and transmission-electron microscopy (TEM) and XRD. To reveal the microstructure, the samples were metallographically polished, followed by etching in 4 volume percent (vol. %) nital solution. The TEM measurements were carried out on JEM-2100 high-resolution transmission electron microscope operated at 200 kV. The plane-view thin foils for TEM were prepared by mechanical grinding, followed by thinning via Gatan PIPS. Phase identification was carried out by X-ray diffraction on a Rigaku D/max-TTR-III diffractometer using Cu Kα.

2.3. Mechanical testing

Tension and compression experiments were performed on an Instron 4505 material tester with a strain rate of ~ 1×10^{-3} s^{-1} at room temperature. An extensometer was used during tension tests. The gauge length, width, and thickness of the tension specimens were 12.5, 4, and 1 mm, respectively. The gauge size for compression tests was 10 mm in diameter and 15 mm in height.

3. Experimental results

3.1. Microstructures

Figure 1 shows the microstructures of the as-cast Mg-3Li-6Al (LA36), Mg-9Li-6Al (LA96), and Mg-15Li-6Al (LA156) (in wt. %) alloys. The LA36 alloy consists of the α phase matrix (hcp) and precipitates (Fig. 1a). The average grain size of the matrix is ~ 40 μm. Most of the precipitates are distributed along grain boundaries. With the Li concentration increasing to 9 wt. %, the LA96 alloy represents a typical duplex phase (hcp + bcc) structure. The phase in the bright color is the hcp α phase and that in gray is the bcc β phase. The morphology of the α phase is an irregular block and long strip, as shown in Fig. 1c. Some small spherical particles are evenly distributed in the β phase (Fig. 1d). For the LA156 alloy, equiaxed grains with an average grain size of ~ 165 μm are shown in Fig. 1e. The precipitate particles are evenly distributed in the grains and gathered along grain boundaries (Fig. 1f).

The X-ray diffraction (XRD) patterns of the as-cast LA36, LA96, and LA156 alloys are illustrated in Fig. 2. The XRD results show that the LA36 alloy consists of the hcp α phase and AlLi phase, the LA96 represents a typical duplex phase of the hcp α phase and bcc β phase as well as AlLi and $MgLiAl_2$ phases, and the LA156 alloy is composed of the bcc β phase, AlLi and $MgLiAl_2$ phases. Clearly, with increasing the Li content, the crystal structure is transformed from the hcp to bcc structures, which is consistent with the Mg-Li phase diagram [7].

The microstructure from scanning electron microscopy (SEM) and the corresponding energy-dispersive spectroscopy (EDS) results of the LA36, LA96, and LA156 alloys are shown in Fig. 3 and Table 1. The SEM images in higher magnification exhibits that the second phases are gathered at the grain boundaries of

the LA36 alloy with an irregular herringbone structure (Fig. 3a). Some small spherical particles with an average size of approximately 1 μm are evenly distributed in the β phase as well as along the α/β boundaries of the LA96 alloy (Fig. 3b). For the LA156 alloys, the precipitate particles are gathered along the grain boundaries; comparatively finer spherical particles with approximately below 1 μm as well as short rod-like precipitates with a width of ~ 0.5 μm and a length of 2 ~ 5 μm are evenly distributed in the grains (Fig. 3c). The corresponding EDS results show that the compounds of the three alloys are composed mainly of Mg and Al elements, as the Li element is too light to be detected by EDS. Combining results of the previous studies and XRD analysis, the second phase in the LA36 alloy ("A" in Fig. 3a) is determined as AlLi [17]. Based on the similar content of Mg and Al elements, it can be inferred that the relatively-large particles in LA96 ("B" in Fig. 3b) and LA156 ("D" in Fig. 3c) are AlLi, and the small size particles in LA96 ("C" in Fig. 3b) and short rod-like precipitates in LA156 ("E' in Fig. 3c) are $MgLiAl_2$.

The transmission-electron microscope (TEM) morphologies and corresponding selected-area electron diffraction (SAED) patterns of the LA36, LA96, and LA156 alloys are shown in Fig. 4. For the LA36 alloy, the corresponding SAED patterns consist of spots from not only the α phase but also the AlLi phase (Fig. 4a). For the LA96 alloy, the corresponding SAED patterns verify the existence of both the AlLi phase and $MgLiAl_2$ phase (Fig. 4b). For the LA156 alloy, $MgLiAl_2$ and AlLi phases (Fig. 4c) are clearly identified. The results further confirm the XRD and SEM analyses of the precipitates.

3.2. Mechanical properties

3.2.1. Tensile properties

The true stress-strain curves of the as-cast LA36, LA96, and LA156 alloys tested at ambient temperature are demonstrated in Fig. 5a, and their tensile properties are listed in Table 2. With increasing the Li addition from 3 to 9 and 15 wt. %, the ultimate tensile strength (UTS) is slightly decreased from 263 to 254 and 237 MPa. However, the tensile yield strength (TYS) is increased from 139 to 161 and 175 MPa, respectively. All the materials have reasonably good tensile ductility. Elongations to facture (E_f) of

the LA36, LA96, and LA156 alloys are ~ 7.1, 16.2, and 11.3%, respectively, implying a better plastic-deformation ability of the duplex structures. As compared to the LA36 (the α phase) , the UTS of LA96 and LA156 decreases while the E_f increases due to the transformation from the hcp to bcc crystal structures and the decrease of lattice constants through the substitution of Mg atoms by Li atoms [18].

Fig. 5b, which is derived from Fig. 5a, presents the Kocks-Mecking type plots of the tensile strain-hardening behaviors of the LA36, LA96, and LA156 alloys tested at room temperature. The plot is illustrated as the tensile strain-hardening rate ($\theta = d\sigma/d\varepsilon$) versus net flow stress (σ - Y), where Y is the (0.2% off-set) yield strength. Apparently, the θ value does not exhibit a certain value after the yield stress. This indicates that there is no stage-II hardening behavior in the present alloys in the Kockse-Mecking type plot, which is mainly related to the low dislocation density in the as-cast samples. The similar experimental results were also reported in the extruded Mg-Sn-Yb alloy sheet [19] and Mg-9Li-1Zn alloy [14]. For the three samples in this study, the strain-hardening rate linearly decreases with increasing the net flow stress, thereby exhibiting stage-III hardening behavior [20, 21], which occurs immediately after yielding. The behavior is very similar to the well-known linear stage-III of strain hardening in face-centered-cubic (fcc) polycrystals [20]. As stage-III appears to approach a saturation level, the new stage-IV gets involved at higher net flow-stress levels in the LA36 and LA96 alloys when the strain-hardening rate has dropped to a particular low level [20-22]. The previous studies [14, 20-23] suggested that the strain-hardening of a material is governed by the evolution rate of the dislocation density, which can be thought of as composed of a dislocation storage (hardening)

component and a dynamic recovery (softening) component related to dislocation annihilation processes. They hypothesized that the hardening component is geometric or statistical in nature, and thus, athermal. While the softening component (or the dynamic recovery) was strongly influenced by thermal activation and, accordingly, temperature and strain rate. The strain-hardening rate accounting for the recovery effects can be expressed as [14, 20-22]:

$$\theta(\sigma - Y) = (\sigma - Y)[\theta_h - \theta_r(\sigma, \dot{\varepsilon}, T)] \quad (1)$$

where θ_h is the athermal component of the strain-hardening rate, θ_r accounts for any softening effects due to dislocation annihilation by dynamic recovery as the temperature and/or the applied stress increase, $\dot{\varepsilon}$ is the strain rate, and T is the temperature. The occurrence of stage-III hardening behavior is generally attributed to dynamic recovery [14, 20-22]. Fig. 5c illustrates the $\theta(\sigma - Y)$ vs. $(\sigma - Y)$ curves for the LA36, LA96, and LA156 alloys. It can be seen that the first part of the curves at low stresses can be fitted by straight lines passing through the origin with a slope θ_h. If an athermal regime of dislocation accumulation exists, a plot of $\theta(\sigma - Y)$ as a function of $(\sigma - Y)$ should begin as a straight line of gradient θ_h passing through the origin [14, 20-22]. The initial hardening behavior of the three alloys in this study is indeed described by homogeneous straight lines, which are similar to those observed for fcc polycrystals [20-22]. The downward curvature of the $\theta(\sigma - Y)$ vs $(\sigma - Y)$ curves at high stresses can be taken as an indication of the onset of dynamic recovery, which corresponds to the declining slope in stress-strain curves [20-22]. Therefore, the earlier onset of dynamic recovery occurs in the LA156, and then in the LA96, and last in the

LA36 alloy, which can be ascribed to the promoting cross-slip and/or dislocation climb by the increasing the Li content.

Figure 6 summarizes the tensile yield strengths (TYS) (a), specific strengths (b), vs elongations to facture (E_f) of various Mg-based cast alloys [10, 24-28]. The as-cast ternary LA36, LA96, and LA156 alloys developed in the present work show better comprehensive mechanical properties (a strength-ductility balance), as compared to the binary Mg-3Li, Mg-9Li [10], and Mg-15Li (in wt. %) alloys and conventional Mg-Al-based alloys [Mg-6Al-1Zn (AZ61) [24], Mg-9Al-1Zn (AZ91D) [25], Mg-4Al-5Zn (AZ45) [26], Mg-9Al-2Sn (AT92) [27], and Mg-8Zn-4Al-xRE (ZA84-xRE) [28] (in wt. %)]. The yield strengths (139, 161, and 175 MPa) and specific strengths (85, 109, and 133 kN m kg^{-1}) of the ternary LA36, LA96, and LA156 alloys are more than twice higher than those [(50, 75, and 65 MPa); (31, 52, and 50 kN m kg^{-1})] of the binary Mg-Li alloy. And the elongations (7.1, 16.2, and 11.3) of the ternary Mg-Li-Al alloy are 2 ~ 5 times greater than those (3 ~ 5.6) of the conventional Mg-Al-based alloys. Besides, the ternary Mg-Li-Al alloys also exhibit the higher yield strengths (139, 161, and 175 MPa) and specific strengths (85, 109, and 133 kN m kg^{-1}) than those [(80 ~ 160 MPa); (45 ~ 88 kN m kg^{-1})] of the conventional Mg-Al-based alloys. Specially, the LA96 alloy shows the best combination of high strength and ductility.

3.2.2. Compression properties

The compressive true stress-strain curves of the as-cast LA36, LA96, and LA156 alloys under compression tests at ambient temperature are shown in Fig. 7, and their compressive properties are listed in Table 3. For the LA36 alloy, the flow stress

increases with increasing strain, and a high strain-hardening is observed. There is an ambiguous elastic-plastic transition. Subsequent continuous hardening immediately occurs after yielding at about 164 MPa. For the LA96 and LA156 alloys, a relatively-distinct yield point is observed before rapid hardening in the plastic region. After yielding at about 176 MPa, the LA96 alloy shows a lower strain-hardening behavior. Moreover, after yielding at about 192 MPa, the LA156 alloy exhibits that a flow stress slightly decreases with further strain, and a strain-softening feature is found.

4. Discussion

The comparison of the tensile yield strengths, specific strengths, and elongations to the facture between various Mg-based cast alloys [10, 24-28] indicates that the as-cast ternary LA36, LA96, and LA156 alloys developed in the present work show better comprehensive mechanical properties (a strength-ductility balance) (Fig. 6). In other words, the alloying with Li to improve ductility and the Al addition to enhance strength are achievable. For the duplex-phase LA96 alloy, the co-existence of the harder hcp-structured α phase and the softer bcc-structured β phase results in a better ductility and proper strength during the tension tests, compared to the other two α/β single-phase alloys. Generally speaking, for the coordinated deformation of the harder α phase and softer β phase, the dislocation slip systems of the two phases do not need to operate simultaneously. The softer β phase is easier to deform, and the harder α phase slips when suffering from the increasing applied force, so as to enable the plastically-compatible deformation of the duplex phases, resulting in comprehensive mechanical properties. The addition of Li in Mg can also induce a decrease in the axial ratio (c/a) of Mg and an increase in the SFE. Hence, slips between crystal planes become easier [8, 9]. Such effect results in the lower strength and higher ductility of the LA156 alloy, as compared to those of the LA36 alloy. This argument is in agreement with the results by Karami and Mahmudi [15]. Also, Al dissolves in both α and β phases, which is expected to strengthen the alloys through solid solutions. The intermetallic particles also play an important role in improving the strength because these particles provide effective barriers to gliding dislocations during deformation.

However, precipitates form a brittle phase and are gathered at grain boundaries. From the microstructures of the LA36, LA96, and LA156 alloys (Figs. 1 and 3), we can see that the particles of the LA36 are in a much larger size and gathered at grain boundaries, leading to a worse ductility. While the particles in the LA96 and LA156 alloys are in a much smaller size and evenly distributed, benefiting to a good ductility.

From the Kocks-Mecking type plots of the tensile strain-hardening behaviors of the LA36, LA96, and LA156 alloys (Fig. 5b), we can see that no stage-II behavior appears in the present alloys in the Kocks-Mecking type plot. As we know, the presence of the stage-II linear hardening behavior is due to the interaction of dislocation in the primary slip system with those in an intersecting slip system, and the dislocation interaction mainly depends on the dislocation density [19]. For the three cast samples in this study, the dislocation density is very low, and thus no stage-II behavior appears. The similar experimental results were also reported in the extruded Mg-Sn-Yb alloy sheet [19] and Mg-9Li-1Zn alloy [14]. For the three samples in this study, the strain-hardening rate linearly decreases with increasing the net flow stress, thereby exhibiting stage-III hardening behavior [20, 21], which occurs immediately after yielding. The behavior is very similar to the well-known linear stage-III of strain hardening in fcc polycrystals [20]. The occurrence of stage-III hardening behavior is generally attributed to dynamic recovery [14, 20-22]. From the Fig. 5c we can see that the earlier onset of dynamic recovery firstly occurs in the LA156, and then occurs in the LA96, and lastly occurs in the LA36 alloy, i.e., dynamic recovery is facilitated with increasing Li content, since all the materials were tested at the same temperature (room temperature). This trend can be ascribed to the promoting cross-slip and/or dislocation

climb by the increasing the Li content, resulting in annihilation of dislocations (the dominant softening process), and thus, decreasing the strain-hardening behavior. As the value of the net flow stress increases, stage-III appears to approach a saturation level, the strain-hardening rate becomes small and steady, and the stage-IV hardening [20-22] occurs at higher net flow-stress levels in the LA36 and LA96 alloys. The mechanism leads to stage-IV is still unclear. Rollett et al. [21] proposed that the hardening rate in stage IV was governed by debris accumulation in the cell walls. The net rate of dislocation accumulation in the major part of stage-III was rather high as compared to that of debris accumulation, while the latter became dominant at the end of stage-III in the new stage-IV where athermal dislocation storage essentially is compensated by dynamic recovery.

The tensile-hardening capacity (H_C^T) of a material can be defined in terms of the ultimate tensile strength (UTS) and yield stress (TYS) as following [22]:

$$(H_C^T) = (UTS - TYS)/TYS = UTS/TYS - 1 \quad (2)$$

The tensile hardening capacities (H_C^T) of the as-cast LA36, LA96, and LA156 alloy are also shown in Table 2. It is evident that increasing the Li content leads to a decrease in the tensile-hardening capacities of the as-cast alloys, from 0.82 to 0.58 and 0.35. This trend might be attributed to the fact that with increasing the Li content, the critical resolved shear stress (CRSS) for non-basal slip diminishes in the hcp α phase [29], resulting in a higher activity of non-basal slip, facilitating the cross-slip between crystal planes and, therefore, decreasing the strain-hardening behavior [18]. Besides, the occurrence of the softer bcc-structured β phase with more independent slip systems, as compared to the hcp-structured α phase, could contribute to the decrease of the strain-hardening behavior [15].

The compressive true stress-strain curves of the alloys (Fig. 7) show that the

LA36 alloy exhibits a high strain-hardening feature with an ambiguous elastic-plastic transition, while the LA96 and LA156 alloys present a lower strain-hardening behavior with relatively-distinct yield points. Moreover, the LA156 alloy exhibits a strain-softening characteristic. It was reported that dislocations accumulated at obstacles contribute to hardening, whereas cross-slip and/or climb of dislocations result in softening [23]. Shang et al. [30] suggests that the Al addition decreases the intrinsic (I_2) stacking-faults energy (SFE), while the Li addition increases this SFE. An increase in the I_2 SFE hinders the extension of basal dislocations whereas promoting cross-slip and/or climb of dislocations [31]. It means that there is a dynamic balance between strain hardening and softening with the Al and Li additions. For the LA36 alloy, the influence of Al, which decreases the I_2 SFE [30], is dominant and reveals high strain-hardening behavior. With further increasing the Li content, which increases the I_2 SFE [30], the influence of Li is dominant and promotes the cross-slip and/or climb of dislocations, which contributes to strain softening.

Unlike cubic metals with symmetrical crystal structures, most hcp-structured Mg alloys exhibit different yield strengths under tension and compression [32]. In particular, wrought Mg alloys tend to display a significant tension-compression yield asymmetry, because of the formation of the strong basal texture and twinning during the fabrication process [33, 34]. For the cast Mg alloy, which is generally considered to have a random texture, the tension-compression yield asymmetry in cast Mg alloys is just related to its twinning behavior in tension and compression [34, 35]. The tension-compression yield asymmetry can be described as the strength differential effect (SDE), and the ratio of the compressive yield strength (CYS) to tensile yield strength (TYS) (asymmetry ratio). The SDE can be calculated as [36, 37]:

$$SDE = 2\frac{|CYS| - |TYS|}{|CYS| + |TYS|} \quad (3)$$

The calculated SDE and asymmetry ratio were given in Table 3. The results show that the CYS is higher than the TYS, and the SDE is positive. On the contrary, most wrought conventional Mg alloys, such as the wrought Mg-3Al-1Zn (AZ31) alloys [38] and extruded Mg-2Mn-1Ce (ME21) alloy [37], exhibit a much more pronounced

negative SDE, and the CYS is significantly lower than TYS. This trend is related to the different deformation modes in wrought alloys during tensile and compressive deformation due to the combined effect of the strong basal texture and the nature of deformation twinning, which can be activated in only one direction, relative to the crystallographic twin plan [33]. It is well known that a high activity of $\{10\bar{1}2\}$ extension twinning occurs in compression along the processing direction, while slip-dominant deformation, particularly the <a> prismatic slip, occurs in tension, parallel to the processing direction [39]. It is also found that $\{10\bar{1}2\}$ extension twinning is activated at a lower CRSS than the <a> prismatic slip. Thus, the extension twinning deformation in compression leads to a significantly low compressive yield strength, while the slip-dominant deformation in tension results in a relatively high yield strength, which leads to a negative SDE [37, 38]. On the other hand, the asymmetric yield behavior of the randomly-textured cast material originates from the difference in $\{10\bar{1}2\}$ twinning characteristics under tensile and compressive loading, because slip-induced deformation is independent of the loading direction [35, 39]. Based on the research of Park et al. [34], the Schmid Factor (SF) values of the $\{10\bar{1}2\}$ twinning system were calculated as a function of the angle, θ, between the loading and c axes, and the maximum value was found to be higher in tension (0.499 at $\theta = 0°$) than in compression (0.437 at $\theta = 90°$) [34, 40, 41]. According to the Schmid's law in the uniaxial loading conditions [42], two aspects imply: (1) CRSS does not depend on the orientation of the load axis, and (2) CRSS is independent of the sign of the loading stress (tension or compression) [43]. The stress required for activating twinning is determined by SF and CRSS (activation stress = CRSS/SF) [34, 42]. Thus, it is evident that $\{10\bar{1}2\}$ twinning activates more easily under tensile loading than compressive loading in cast Mg alloys, and thus, the tensile yield strength is lower than compressive yield strength as well as a positive SDE. The asymmetry ratio and SDE value of the LA36 (1.180 and 0.165, respectively) are higher than those of the LA96 (1.093 and 0.089) and LA156 (1.097 and 0.093), implying a lower tension-compression yield

asymmetry with increasing the Li addition. Several researchers have proved that the addition of Li into the Mg alloy will result in increasing the CRSS of the <a> basal slip and extension twinning and decreasing the CRSS of non-basal slips, such as the <a> prismatic slip and <c + a> pyramidal slip [8-10, 35, 44-46]. That is to say, with increasing the Li addition, the CRSS of $\{10\bar{1}2\}$ extension twinning improves, which is the inverse cause for the higher tensile yield strength or compressive yield strength.

5. Conclusions

Cast Mg-Li-Al alloys with comprehensive mechanical properties (a strength-ductility balance) are successfully developed by introducing the duplex (hcp + bcc) phases and fine intermetallic particles. The yield strength of ~ 175 MPa, specific strength of ~ 133 kN m kg^{-1} of the ternary Mg-9Li-6Al alloy with the duplex (hcp + bcc) structures are obtained, which are more than twice higher than those of the binary Mg-Li alloy. The elongation of ~ 16.2% is 2 ~ 5 times greater than those of the conventional Mg-Al-based alloys. With increasing the Li addition from 3 to 9 and 15 wt. %, the tensile strain-hardening capacity decreases from 0.89 to 0.58 and 0.35 and the asymmetry ratio decreases from 1.180 to 1.093 and 1.097, respectively. These findings offer insights into the enhancement of comprehensive mechanical properties (strength and ductility), and have important implications in developing novel superlight Mg alloys.

Acknowledgments

This work was supported by the NSFC Funding (51371062, and U1460102), NSFHLJ (JC2017012), the Scientific Research Foundation for the Returned Overseas Chinese Scholars (Heilongjiang Province) and the Fundamental Research Funds for the Central Universities (HEUCFJ171005, HEUCFJ171001 and HEUCFP201703). HB was supported by the U.S. Department of Energy, Office of Sciences, Basic Energy Science, Materials Science and Engineering Division. PKL would like to acknowledge the Department of Energy (DOE), Office of Fossil Energy, National Energy Technology Laboratory (DE-FE-0008855 and DE-FE-0024054, and DE-FE-0011194), with Mr. V. Cedro and Mr. R. Dunst as program managers. PKL

ACCEPTED MANUSCRIPT

thanks the support from the project of DE-FE-0011194 with the program manager, Dr. J. Mullen. PKL very much appreciates the support of the U.S. Army Research Office project (W911NF-13-1-0438) with the program manager, Dr. D. M. Stepp. TE was supported by the Department of Energy, Office of Sciences, Basic Energy Sciences, Materials Science and Engineering Division. PKL thanks the support from the National Science Foundation (CMMI-1100080 and DMR-1611180) with the program directors, Drs. C. Cooper and D. Farkas.

ACCEPTED MANUSCRIPT

References

[1] Z.X. Wu, W.A. Curtin, The origins of high hardening and low ductility in magnesium, Nature 526, (2015) 62-67.

[2] L. Wu, A. Jain, D.W. Brown, G.M. Stoica, S.R. Agnew, B. Clausen, D.E. Fielden, P.K. Liaw, Twinning-detwinning behavior during the strain-controlled low-cycle fatigue testing of a wrought magnesium alloy, ZK60A, Acta Mater. 56 (2008) 688-695.

[3] L. Wu, S.R. Agnew, D.W. Brown, G.M. Stoica, B. Clausen, A. Jain, D.E. Fielden, P.K. Liaw, Internal stress relaxation and load redistribution during the twinning-detwinning-dominated cyclic deformation of a wrought magnesium alloy, ZK60A, Acta Mater. 56 (2008) 3699-3707.

[4] W.Q. Xu, N. Birbilis, G. Sha, Y. Wang, J.E. Daniels, Y. Xiao, M. Ferry, A high-specific-strength and corrosion-resistant magnesium alloy, Nat. Mater. 14 (2015) 1229-1235.

[5] R.Z. Wu, Y.D. Yan, G.X. Wang, L.E. Murr, W. Han, Z.W. Zhang, M.L. Zhang, Recent progress in magnesium-lithium alloys, Int. Mater. Rev. 60 (2015) 65-100.

[6] I. Shin, E.A. Carter, First-principles simulations of plasticity in body-centered-cubic magnesium-lithium alloys, Acta Mater. 64 (2014) 198-207.

[7] T.B. Massalski (Ed.), Binary Alloy Phase Diagrams, ASM, Metals Park, OH, 1986.

[8] M. Lentz, M. Klaus, I.J. Beyerlein, M. Zecevic, W. Reimers, M. Knezevic, In situ X-ray diffraction and crystal plasticity modeling of the deformation behavior of extruded Mg-Li-(Al) alloys: An uncommon tension-compression asymmetry, Acta Mater. 86 (2015) 254-268.

[9] J.A. Yasi, L.G. Hector, D.R. Trinkle, Prediction of thermal cross-slip stress in magnesium alloys from a geometric interaction model, Acta Mater. 60 (2012) 2350-2358.

[10] Y. Zou, L.H. Zhang, H.T. Wang, X. Tong, M.L. Zhang, Z.W. Zhang, Texture evolution and their effects on the mechanical properties of duplex Mg–Li alloy, J. Alloys Compd. 669 (2016) 72-78.

[11] Y. H. Kim, J. H. Kim, H. S. Yu, J. W. Choi, H. T. Son, Microstructure and mechanical properties of Mg-xLi-3Al-1Sn-0.4 Mn alloys (x= 5, 8 and 11wt%), J. Alloys Compd. 583 (2014) 15-20.

[12] Z. Chen, Z. Li, C. Yu, Hot deformation behavior of an extruded Mg-Li-Zn-RE alloy, Mater. Sci. Eng. A 528 (2011) 961-966.

[13] Z. Trojanová, Z. Drozd, P. Lukáč, F. Chmelík, Deformation behaviour of Mg-Li alloys at elevated temperatures, Mater. Sci. Eng. A (2005) 148-151.

[14] H.Y. Wu, J.C. Yan, H.H. Tsai, C.H. Chiu, G.Z. Zhou, C.F. Lin, Tensile flow and strain-hardening behaviors of dual-phase Mg-Li-Zn alloy thin sheets, Mater. Sci. Eng. A 527 (2010) 7197-7203.

[15] M. Karami, R. Mahmudi, Work hardening behavior of the extruded and equal-channel angularly pressed Mg-Li-Zn alloys under tensile and shear deformation modes, Mater. Sci. Eng. A 607 (2014) 512-520.

[16] H.Y. Wu, J.Y. Lin, Z.W. Gao, H.W. Chen, Effects of age heat treatment and thermomechanical processing on microstructure and mechanical behavior of LAZ1010 Mg alloy, Mater. Sci. Eng. A 523 (2009) 7-12.

[17] Z.K. Qu, R.Z. Wu, H.B. Zhan, M.L. Zhang, The solution and room temperature aging behavior of Mg-9Li-xAl(x=3, 6) alloys, J. Alloys Compd. 536 (2012) 145-149.

[18] Z. Drozd, Z. Trojanová, S. Kúdela, Deformation behaviour of Mg-Li-Al alloys, J. Alloys Compd. 378 (2004) 192-195.

[19] J. Jiang, G. Bi, G. Wang, Q. Jiang, J. Lian, Z. Jiang, Strain-hardening and warm deformation behaviors of extruded Mg-Sn-Yb alloy sheet, J. Magnes. Alloy. 2 (2014) 116-123.

[20] U.F. Kocks, H. Mecking, Physics and phenomenology of strain hardening: the FCC case, Prog. Mater. Sci. 48 (2003) 171-273.

[21] A. Rollett, U. Kocks, R. Doherty. Stage IV work hardening in cubic metals. Los Alamos National Lab., NM (USA); Drexel Univ., Philadelphia, PA (USA), 1986.

[22] N. Afrin, D.L. Chen, X. Cao, M. Jahazi, Strain hardening behavior of a friction stir welded magnesium alloy, Scr. Mater. 57 (2007) 1004-1007.

[23] P. Lukáč, Z. Trojanová. Hardening and softening in magnesium alloys, Magnesium Alloys-Design, Processing, and Properties, (2011) 1-20.

[24] M. Yang, F. Pan, R. Cheng, S. Jia, Comparison about effects of Sb, Sn and Sr on as-cast microstructure and mechanical properties of AZ61-0.7Si magnesium alloy, Mater. Sci. Eng. A 489 (2008) 413-418.

[25] A.S. Handbook. Magnesium and magnesium alloys.

[26] J.M. Kim, B.K. Park, J.H. Jun, K.T. Kim, W.J. Jung, Microstructure and mechanical properties of cast and semi-solid formed Mg-Al-Zn alloys. Solid State Phenom. 116 (2006) 288-291.

[27] T. Zhu, P. Fu, L. Peng, X. Hu, S. Zhu, W. Ding, Effects of Mn addition on the microstructure and mechanical properties of cast Mg-9Al-2Sn (wt.%) alloy, J. Magnes. Alloy. 2 (2014) 27-35.

[28] Y.X. Wang, S.K. Guan, X.Q. Zeng, W.J. Dine, Effects of RE on the microstructure and mechanical properties of Mg-8Zn-4Al magnesium alloy, Mater. Sci. Eng. A 416 (2006) 109-118.

[29] H. Yoshinaga, R. Horiuchi, On the flow stress of α solid solution Mg-Li alloy single crystals, Trans. JIM 4 (1963) 134-141.

[30] S.L. Shang, W.Y. Wang, B.C. Zhou, Y. Wang, K.A. Darling, L.J. Kecskes, S.N. Mathaudhu, Z.K. Liu, Generalized stacking fault energy, ideal strength and twinnability of dilute Mg-based alloys: A first-principles study of shear deformation, Acta Mater. 67 (2014) 168-180.

[31] Q. Zhang, L. Fu, T.W. Fan, B.Y. Tang, L.M. Peng, W.J. Ding, Abinitio study of the effect of solute atoms Zn and Y on stacking faults in Mg solid solution, Physica B 416 (2013) 39-44.

[32] C. Roberts. Magnesium and its Alloys, New York,Wiley, 1960.

[33] E. Ball, P. Prangnell, Tensile-compressive yield asymmetries in high strength wrought magnesium alloys, Scr. Metall. Mater. 31 (1994) 111-116.

[34] S.H. Park, J.H. Lee, B.G. Moon, B.S. You, Tension-compression yield asymmetry in as-cast magnesium alloy, J. Alloys Compd. 617 (2014) 277-280.

[35] S.R. Agnew, M.H. Yoo, C.N. Tomé, Application of texture simulation to understanding mechanical behavior of Mg and solid solution alloys containing Li or Y, Acta Mater. 20 (2001) 4277-4289.

[36] T.B. Stoughton, J.W. Yoon, A pressure-sensitive yield criterion under a non-associated flow rule for sheet metal forming, Int. J. Plast. 20 (2004) 705-731.

[37] M. Huppmann, S. Gall, S. Mueller, W. Reimers, Changes of the texture and the mechanical properties of the extruded Mg alloy ME21 as a function of the process parameters, Mater. Sci. Eng. A 528 (2010) 342-354.

[38] M. Huppmann, W. Reimers, Microstructure and mechanical properties of differently extruded AZ31 magnesium alloy, Int. J. Mater. Res. 101 (2010) 1264-1271.

[39] S. Xu, V. Gertsman, J. Li, J. Thomson, M. Sahoo, Role of mechanical twinning in tensile compressive yield asymmetry of die cast Mg alloys, Can. Metall. Q. 44 (2005) 155-166.

[40] S.G. Hong, S.H. Park, C.S. Lee, Role of {10-12} twinning characteristics in the deformation behavior of a polycrystalline magnesium alloy, Acta Mater. 58 (2010) 5873-5885.

[41] S.H. Park, S.G. Hong, C.S. Lee, In-plane anisotropic deformation behavior of rolled Mg-3Al-1Zn

alloy by initial {10-12} twins, Mater. Sci. Eng. A 570 (2013) 149-163.
[42] J.L. Bassani, Plastic flow of crystals, Adv. Appl. Mech. 30 (1994) 192-259.
[43] V. Bulatov, O. Richmond, M. Glazov, An atomistic dislocation mechanism of pressure-dependent plastic flow in aluminum, Acta Mater. 47 (1999) 3507-3514.
[44] E. Kelley, W. HOSFORD, Plane-strain compression of magnesium and magnesium alloy crystals, Trans. Met. Soc. AIME 242 (1968) 5-13.
[45] S. Sandlöbes, Z. Pei, M. Friák, L.F. Zhu, F. Wang, S. Zaefferer, D. Raabe, J. Neugebauer, Ductility improvement of Mg alloys by solid solution: Ab initio modeling, synthesis and mechanical properties, Acta Mater. 70 (2014) 92-104.
[46] S.R. Agnew, J.A. Horton, M.H Yoo, Transmission electron microscopy investigation of< c+ a> dislocations in Mg and α-solid solution Mg-Li alloys, Metall. Mater. Trans. A 33 (2002) 851-858.

Tables

Table 1. EDS results of the LA36, LA96, and LA156 alloys. The “A, B, C, D, and E” marked in Fig. 3 are the locations where the EDS measurements were performed.

Element / Number	wt. %		at. %	
	Mg	Al	Mg	Al
A	86.6	13.4	87.8	12.2
B	87.2	12.8	88.3	11.7
C	97.6	2.4	97.8	2.2
D	86.4	13.6	87.6	12.4
E	94.3	5.7	94.9	5.1

Note: the Li element wasn’t involved in the table because the Li element is too light to be detected by EDS.

ACCEPTED MANUSCRIPT

ACCEPTED MANUSCRIPT

Table 2. Tensile properties of the as-cast LA36, LA96, and LA156 alloys.

Alloy	TYS (MPa)	UTS (MPa)	E_f (%)	specific strength (kN m kg^{-1})	H_C^T
LA36	139 ± 5	263 ± 5	7.1 ± 0.5	85	0.89
LA96	161 ± 5	254 ± 5	16 ± 1	109	0.58
LA156	175 ± 5	237 ± 5	11 ± 1	133	0.35

ACCEPTED MANUSCRIPT

Table 3. The tension-compression yield asymmetry specified by the tension (TYS) and the compression (CYS) yield strength, asymmetry ratio (CYS/TYS), and the strength differential effect (SDE) of the cast alloys.

Alloy	TYS (MPa)	CYS (MPa)	CYS/TYS	SDE
LA36	139 ± 5	164 ± 10	1.180	0.165
LA96	161± 5	176 ± 10	1.093	0.089
LA156	175± 5	192 ± 10	1.097	0.093

ACCEPTED MANUSCRIPT

Figure captions:

Fig. 1. Optical micrographs of the LA36 (a,b), LA96 (c,d), and LA156 (e,f) alloys.

Fig. 2. XRD patterns of the LA36, LA96, and LA156 alloys.

Fig. 3. SEM morphologies of the LA36 (a), LA96 (b), and LA156 (c) alloys. The "A, B, C, D, and E" marked in figures are the locations where the EDS measurements were performed.

Fig. 4. TEM images of the LA36 (a), LA96 (b), and LA156 (c, d) alloys and the corresponding SAED insets, respectively.

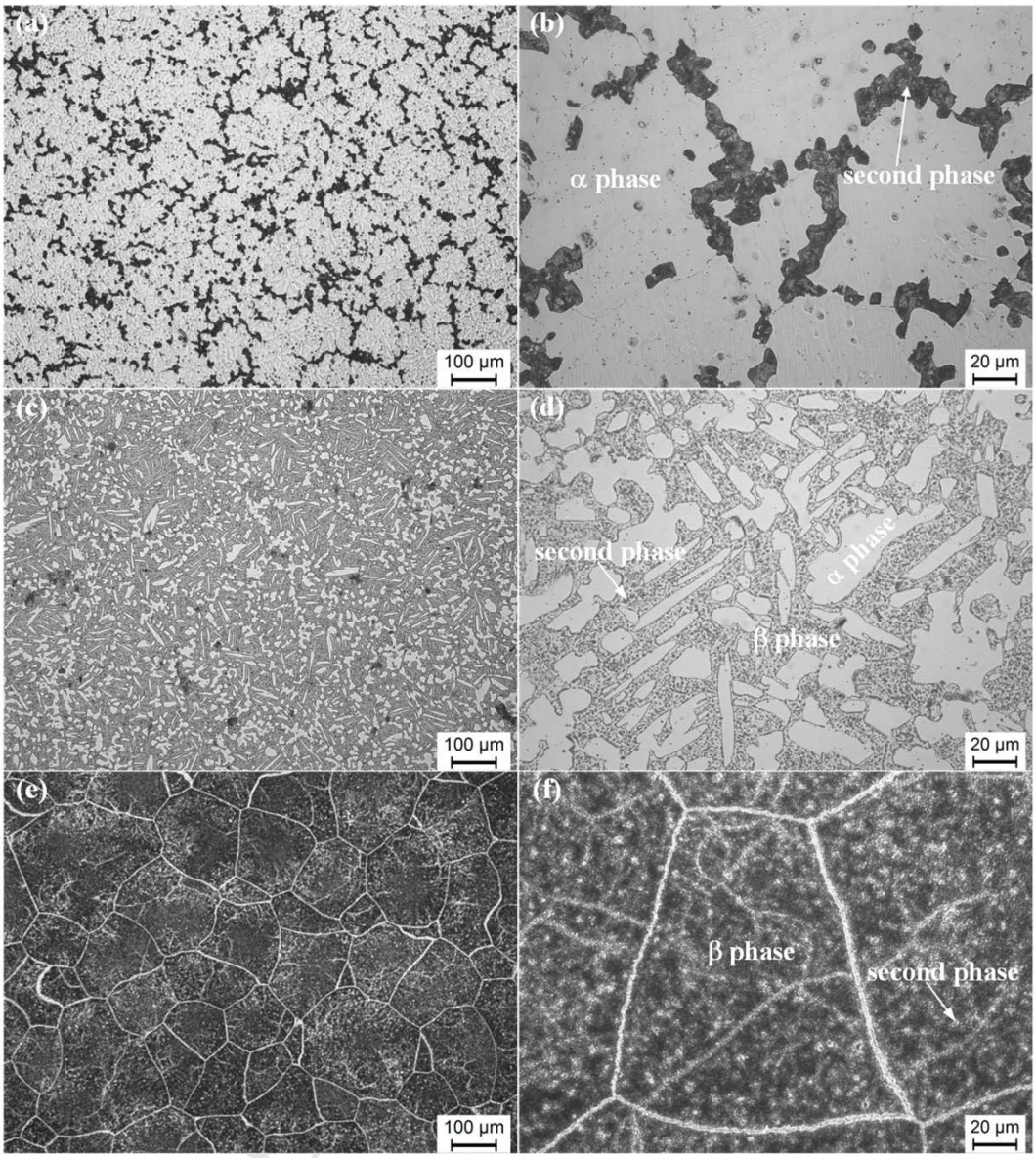
Fig. 5. The tensile true strain-stress curves (a), Kocks-Mecking plots (b), and $\theta(\sigma - Y)$ vs. $(\sigma - Y)$ curves (c) of the LA36, LA96, and LA156 alloys.

Fig. 6. Comparative studies on the tensile yield stress (a) and specific stress (b) vs elongation to failure of various Mg-based cast alloys.

Fig. 7. The compressive true stress-strain curves of the LA36, LA96, and LA156 alloys.

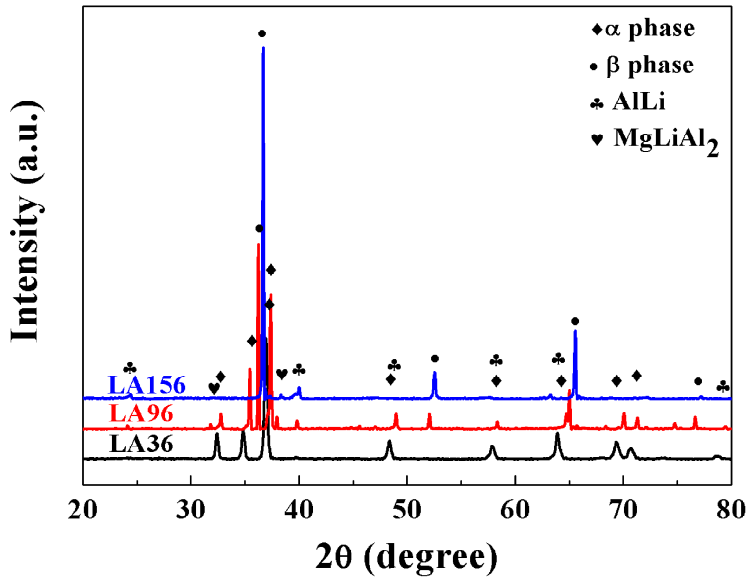
ACCEPTED MANUSCRIPT

Fig. 1



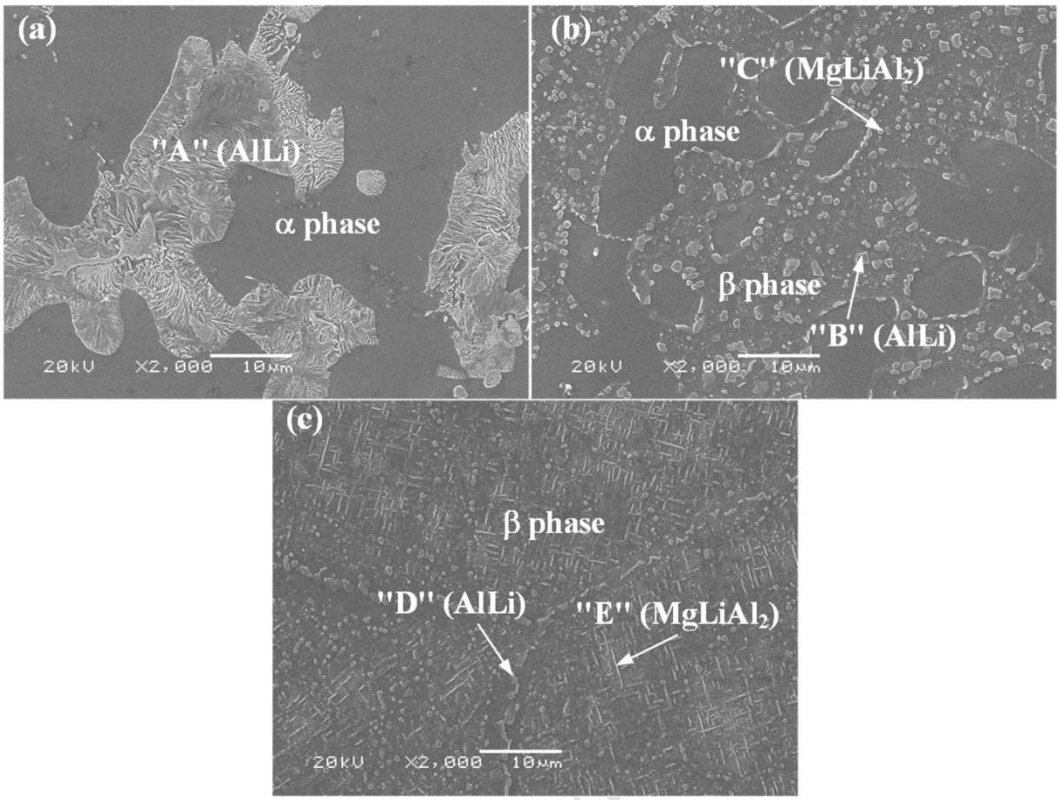
ACCEPTED

Fig. 2



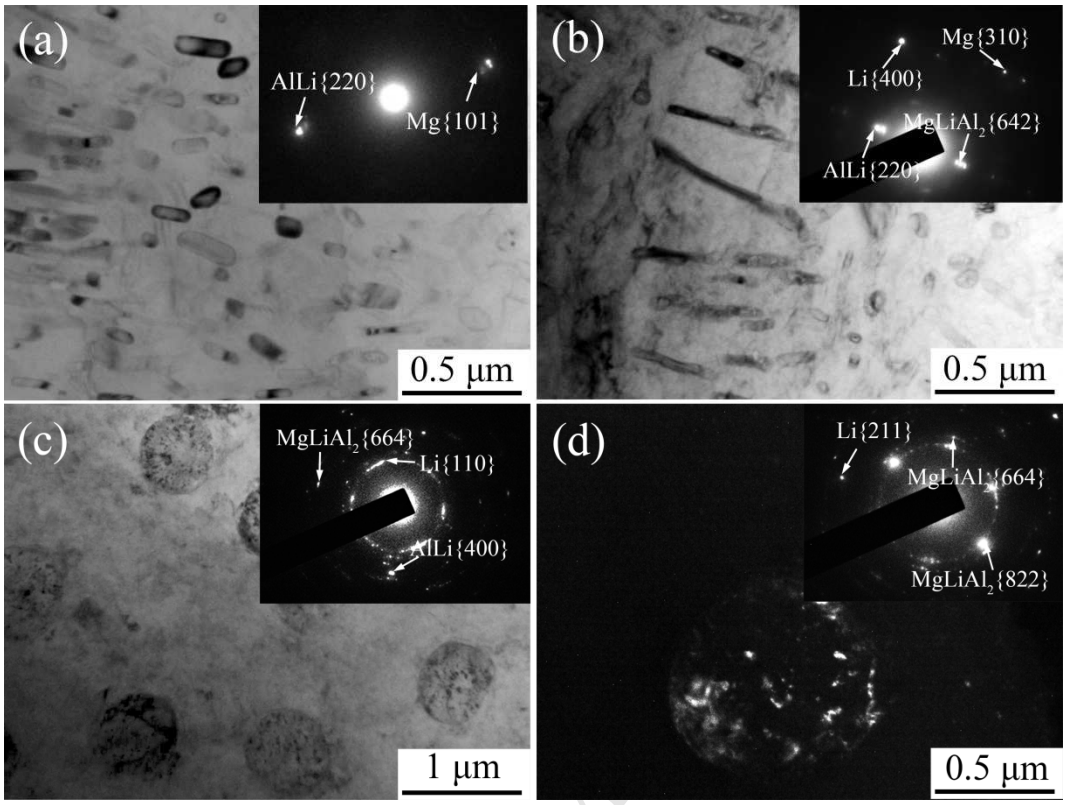
ACCEPTED MANUSCRIPT

Fig. 3



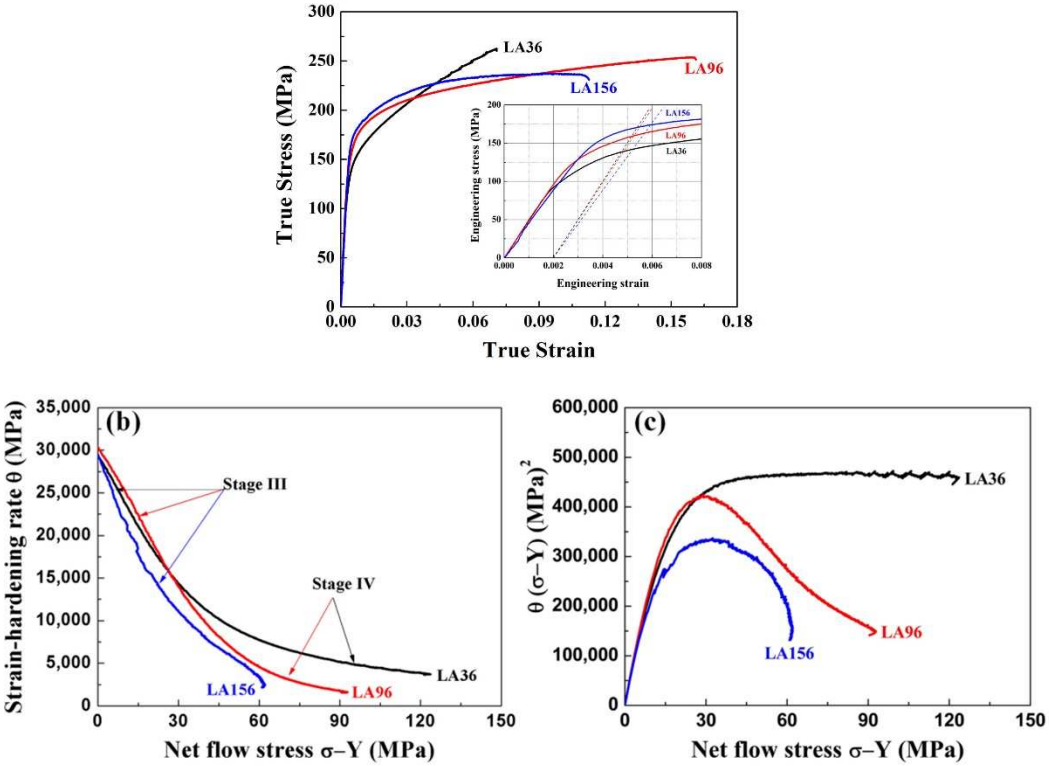
ACCEPTED MANUSCRIPT

Fig. 4



ACCEPTED MANUSCRIPT

Fig. 5



ACCEPTED MANUSCRIPT

Fig. 6

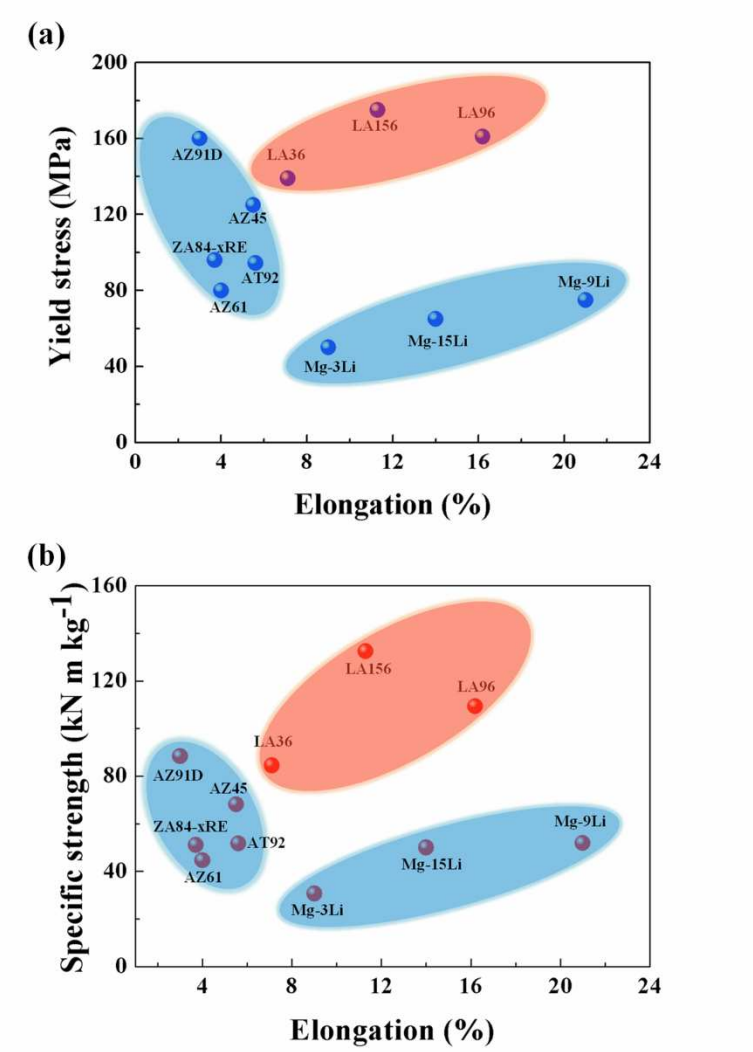
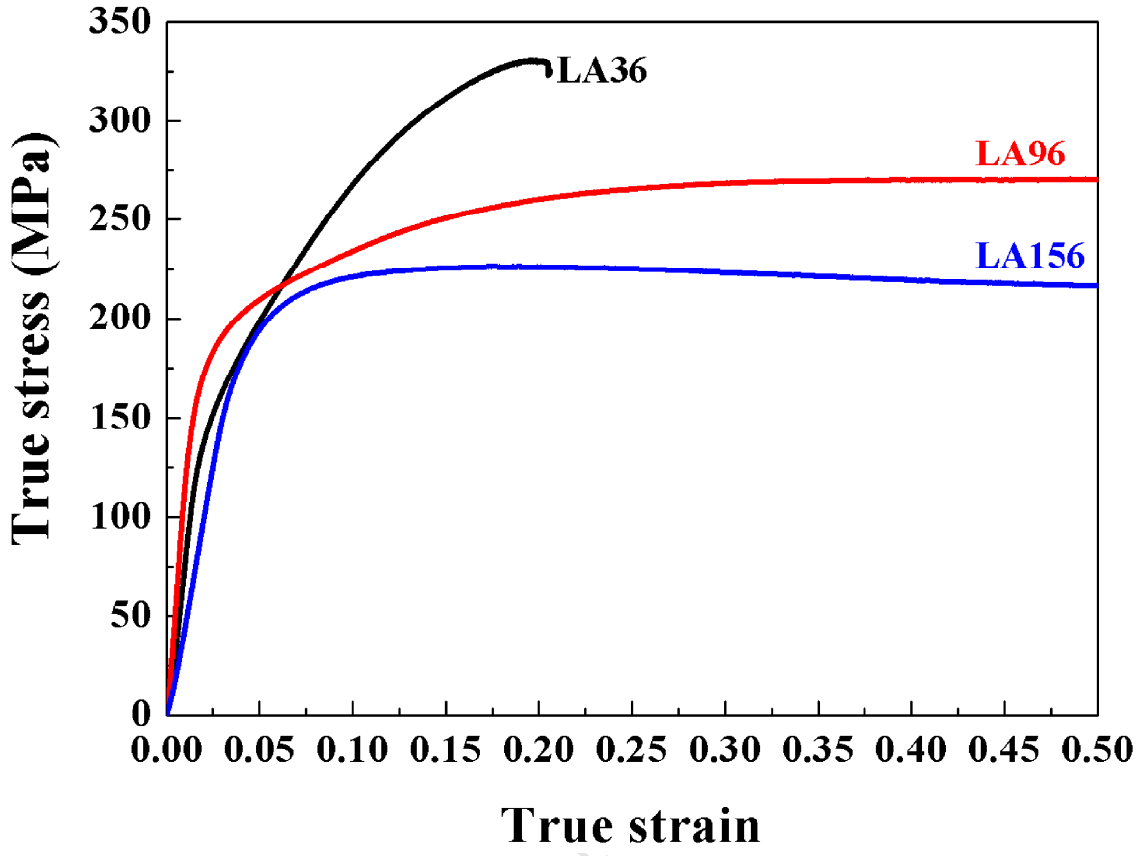

(a)
Yield stress (MPa)
Elongation (%)
AZ91D
LA156
LA96
LA36
AZ45
ZA84-xRE
AT92
AZ61
Mg-9Li
Mg-15Li
Mg-3Li
(b)
Specific strength (kN m kg-1)
Elongation (%)
LA156
LA96
LA36
AZ91D
AZ45
ZA84-xRE
AT92
AZ61
Mg-9Li
Mg-15Li
Mg-3Li

Fig. 7



ACCEPTED MANUSCRIPT

ACCEPTED MANUSCRIPT

Highlights

1. The Mg-Li-Al alloys show better mechanical properties, as compared to various Mg-based alloys.
2. Mechanical properties of Mg-Li-Al alloys can be improved significantly by duplex structure and fine intermetallic particles.
3. The work-hardening rates of Mg-Li-Al alloys were found to decrease with increasing the Li content.

ACCEPTED MANUSCRIPT